New nonlinear mechanisms of midlatitude atmospheric low-frequency variability

A.E. Sterk [a,*], R. Vitolo [b], H.W. Broer [a], C. Simó [c], H.A. Dijkstra [d]

[a] Johann Bernoulli Institute for Mathematics and Computer Science, University of Groningen, PO Box 407, 9700 AK Groningen, The Netherlands
[b] School of Engineering, Computing and Mathematics, University of Exeter, North Park Road, Exeter, EX4 4QF, United Kingdom
[c] Departament de Matemàtica Aplicada i Anàlisi, Universitat de Barcelona, Gran Via 585, 08007 Barcelona, Spain
[d] Institute for Marine and Atmospheric Research Utrecht, Utrecht University, Princetonplein 5, 3584 CC Utrecht, The Netherlands

ABSTRACT

This paper studies the dynamical mechanisms potentially involved in the so-called atmospheric low-frequency variability, occurring at midlatitudes in the Northern Hemisphere. This phenomenon is characterised by recurrent non-propagating and temporally persistent flow patterns, with typical spatial and temporal scales of 6000–10 000 km and 10–50 days, respectively.

We study a low-order model derived from the 2-layer shallow-water equations on a β-plane channel. The main ingredients of the low-order model are a zonal flow, a planetary scale wave, orography, and a baroclinic-like forcing.

A systematic analysis of the dynamics of the low-order model is performed using techniques and concepts from dynamical systems theory. Orography height (h_0) and magnitude of zonal wind forcing (U_0) are used as control parameters to study the bifurcations of equilibria and periodic orbits. Along two curves of Hopf bifurcations an equilibrium loses stability ($U_0 \geq 12.5$ m/s) and gives birth to two distinct families of periodic orbits. These periodic orbits bifurcate into strange attractors along three routes to chaos: period doubling cascades, breakdown of 2-tori by homo- and heteroclinic bifurcations, or intermittency ($U_0 \geq 14.5$ m/s and $h_0 \geq 800$ m).

The observed attractors exhibit spatial and temporal low-frequency patterns comparing well with those observed in the atmosphere. For $h_0 \leq 800$ m the periodic orbits have a period of about 10 days and patterns in the vorticity field propagate eastward. For $h_0 \geq 800$ m, the period is longer (30–60 days) and patterns in the vorticity field are non-propagating. The dynamics on the strange attractors are associated with low-frequency variability: the vorticity fields show weakening and strengthening of non-propagating planetary waves on time scales of 10–200 days. The spatio-temporal characteristics are "inherited" (by intermittency) from the two families of periodic orbits and are detected in a relatively large region of the parameter plane. This scenario provides a characterisation of low-frequency variability in terms of intermittency due to bifurcations of waves.

1. Introduction

Weather and climate are complex natural systems since they involve many temporal and spatial scales and a large number of physical processes. In this paper we restrict our attention to large-scale atmospheric flows on time scales of several days to weeks.

1.1. Statement of the problem

A classical problem in the theory of General Atmospheric Circulation is the characterisation of the recurrent flow patterns observed at midlatitudes in the northern hemisphere winters [1]. This issue has been subject of much scientific attention at least since Baur's definition of *Grosswetterlagen* [2], or Rex's description of Atlantic blocking [3]. One of the motivations for the interest is the potential importance of this problem to understand the persistence and predictability of atmospheric motion beyond the time scales of baroclinic synoptic disturbances (2 to 5 days). Indeed, it is expected that insight into the nature of *low-frequency regime dynamics* will lead to significant progress in the so-called

* Corresponding author. Tel.: +31 0 50 363 3992; fax: +31 0 50 363 3800.
E-mail addresses: a.e.sterk@rug.nl (A.E. Sterk), r.vitolo@ex.ac.uk (R. Vitolo), h.w.broer@rug.nl (H.W. Broer), carles@maia.ub.es (C. Simó), dijkstra@phys.uu.nl (H.A. Dijkstra).

extended range weather forecasting [4]. At the same time, the problem is of great relevance in climate science, since it has been proposed that climate change predominantly manifests itself through changes in the atmospheric circulation regimes, that is "changes in the PDF (probability distribution function) of the climate attractor" [5]. As a matter of fact, misrepresentation of the statistics of blocking and planetary waves is widespread in climate models [6,7]: this may have a profound impact on the ability of such models to reproduce both current climate and climate change.

There are various approaches to the problem of low-frequency atmospheric variability and they are not equivalent—though not independent of each other. An old theory associates recurrent large-scale flow patterns with stationary states of the atmospheric circulation, which correspond to equilibria in the dynamical equations of atmospheric motion. Small-scale weather acts then as a random perturbation inducing fluctuations around equilibria and transitions between states. This mechanism would be responsible for the existence of multimodal statistics in observed data, like the bimodal distribution of planetary activity on zonal wavenumbers 2, 3, 4 found by Hansen and Sutera [8].

Orographic resonance theories lend support to the hypothesis that activity of planetary waves possesses a multimodal distribution [9]. A seminal paper in this direction was that by Charney and DeVore in 1979 [10]: they proposed that the interaction between zonal flow and wave field via form-drag causes the occurrence of two equilibria for the amplitude of planetary waves. This idea was further elaborated by Legras and Ghil [11] who found intermittent transitions between multiple equilibria representing blocked and zonal flows. Crommelin and co-workers [12–14] explain the transitions in terms of homo- and heteroclinic dynamics near equilibria corresponding to distinct preferred flow patterns. More recent developments [15] aimed at theories allowing for multiple stable equilibria at the same zonal wind speed, in such a way that the amplitudes of the corresponding ultralong (planetary scale) waves differ by values of the order of 100 m of geopotential height.

Despite this remarkable research effort, the scientific debate is still very much open on whether a single equilibrium/mode [16–18] or multiple equilibria/modes [19,10,20–22] characterise the large-scale atmospheric circulation.

Spectral analysis is an alternative way of characterising low-frequency atmospheric variability. Examination of the so-called Hayashi spatio-temporal spectra show that the low-frequency component of the variance of the 500 mb geopotential heights is concentrated in the region of periods larger than 10 days and zonal wavenumbers less than 5 [23]. Benzi and Speranza [19] re-examine previous studies of amplification of waves with zonal wavenumber 3 [24] and of onset of Pacific anomalies [25]. They summarise the main physical features of low-frequency atmospheric variability:

- it is on average almost totally non-propagating; planetary waves show a slight tendency to propagate westwards for wavenumbers 1–2 and eastwards for wavenumber 4;
- it seems related to ultralong wave amplification through a non-standard form of baroclinic instability in which orography plays an essential role;
- it is characterised by vertical coherence of the anomalies (e.g. Figs. 9–10 of [25]).

Hansen and Sutera [8] hypothesise a baroclinic conversion process balancing dissipation at wavenumbers 2, 3, 4, which is not associated to the ordinary baroclinic instability, given the equivalent barotropic nature of the difference fields between the two modes of their wave indicator. It has been known since Charney and Eliassen's work [26] that the interaction between eddy field and orography on planetary scales is characterised by a non-propagating amplification of the eddy field: this is one of the common features observed in many studies of transitions between regimes (see e.g. [27] and references therein).

The central question debated here is: does the atmospheric variability characterising the Northern Hemisphere midlatitude circulation result from dynamical processes specific to the interaction of zonal flow and planetary waves with orography, and what are these processes?

1.2. Our approach

We derive a "minimal model" for the midlatitude atmospheric circulation, containing the essential "ingredients" to capture the basic features of low-frequency variability: zonal flow, a large-scale planetary wave, orography, and a baroclinic-like forcing. The model is obtained by Galerkin projection of the 2-layer shallow-water equations onto a small number of spatial modes: in the zonal direction we select wavenumbers $m = 0$ (for the zonal flow) and $m = 3$ (for the large-scale wave). The latter is chosen because it is where the maximum of the low-frequency stationary variance is attained, see e.g. Fig. 2 in [23]. We retain wavenumbers 0, 1, 2 in the meridional direction. The basic idea is to search for dynamical processes inherent to the largest spatial scales, using a conceptual model which is sufficiently simple for this purpose. We do not aim at a realistic representation of atmospheric motion, although our modelling approach is motivated by the observational evidence discussed in the previous section. We return to this point at the end of Section 4.
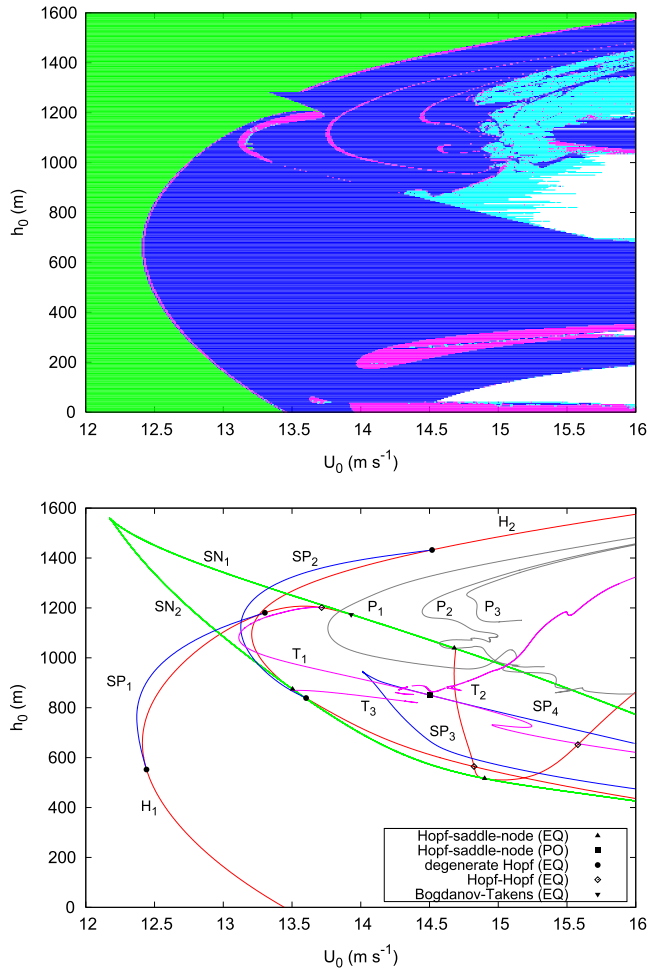
The full shallow-water equations are a system of 6 partial differential equations for the horizontal velocity field u_ℓ, v_ℓ and thickness h_ℓ for $\ell = 1, 2$. Forcing is modelled as relaxation to an apparent westerly wind and orography is included in the bottom layer. Orography height and the forcing zonal wind strength are controlled by parameters h_0 and U_0 respectively. Working with a shallow-water model, instead of the more traditional quasi-geostrophic models, offers the advantage that physically relevant values can be used for h_0: this parameter is bound to be small in the quasi-geostrophic models traditionally used to study low-frequency variability, due to the perturbative nature of orography in quasi-geostrophic theory (see e.g. [28]).

1.3. Summary of the results

The major achievement in this work is to propose a characterisation of low-frequency atmospheric behaviour in terms of intermittency due to bifurcations of waves. Non-propagating planetary waves arise in our model from the interaction of zonal flow with orography. The waves are associated to mixed baroclinic/barotropic instabilities, where the baroclinicity is not that associated to midlatitude synoptic systems (indeed, wavenumber 3 is not the most unstable baroclinic mode). Rather, instabilities here bear resemblance to the orographic baroclinic instability (see [29] and references therein).

Low-frequency behaviour with the appropriate time scales (10–200 days, where the lower-frequency components of 60–200 days can be interpreted as harmonics of the higher-frequency components of 10–60 days) is exhibited by our "minimal model" for physically relevant values of the parameters ($U_0 \approx 15$ m/s and $h_0 \approx 1000$ m). Here, the dynamics of our minimal model takes place on strange attractors which are formed through sequences of bifurcations of periodic orbits (waves) as the forcing wind speed U_0 increases.

The model dynamics is stationary for $U_0 \leq 12.2$ m/s due to the presence of a stable equilibrium corresponding to a steady westerly wind. This steady flow becomes unstable through Hopf bifurcations (associated with mixed baroclinic/barotropic instabilities) as the forcing U_0 increases. This gives rise to two types of stable waves: for lower orography (about 800 m), the period is about 10 days and there is eastward propagation in the bottom

Table 1
Colour coding for the Lyapunov diagram and bifurcation diagram in Fig. 1.

Colour	Lyapunov exponents	Attractor type
Green	$0 > \lambda_1 \geq \lambda_2 \geq \lambda_3$	Equilibrium
Blue	$\lambda_1 = 0 \geq \lambda_2 \geq \lambda_3$	Periodic orbit
Magenta	$\lambda_1 = \lambda_2 = 0 > \lambda_3$	2-torus
Cyan	$\lambda_1 > 0 \geq \lambda_2 \geq \lambda_3$	Strange attractor
White		Escaping orbit

Colour	Bifurcation type	Bifurcating attractor
Green	Saddle-node bifurcation	Equilibrium
Red	Hopf bifurcation	Equilibrium
Magenta	Hopf–Neĭmark–Sacker bifurcation	Periodic orbit
Grey	Period doubling bifurcation	Periodic orbit
Blue	Saddle-node bifurcation	Periodic orbit

Fig. 1. Top: Lyapunov diagram for the attractors of the system (see Appendix A.2 for the algorithm used here). Bottom: bifurcation diagram of attractors of the low-order model in the (U_0, h_0) parameter plane, same parameter window as above (see Appendix A for the algorithm). The marked locations are codimension-2 bifurcations. See Table 1 for the colour coding. (For interpretation of the references to colour in this figure legend, the reader is referred to the web version of this article.)

layer; for more pronounced orography, the period is longer (30–60 days) and the waves are non-propagating. These waves remain stable in relatively large parameter domains and bifurcate into strange attractors through a number of scenarios (see below) in the parameter quadrant $U_0 \geq 14.5$ m/s and $h_0 \geq 850$ m. The dynamics on these strange attractors is associated with irregularly recurring vorticity patterns, which are inherited from the periodic orbit that gives birth to the strange attractor.

The Lyapunov diagram (top panel of Fig. 1) shows a classification of the dynamical behaviour in the different regions of the (U_0, h_0)-plane. Bifurcations of equilibria and periodic orbits (bottom panel) explain the main features of the Lyapunov diagram (see Appendix A for the algorithms). The two Hopf curves $H_{1,2}$ give birth to stable periodic orbits. In turn, these periodic orbits bifurcate into strange attractors through three main routes to chaos:

- Period doubling cascade of periodic orbits (the curves $P_{1,2,3}$);
- Hopf–Neĭmark–Sacker bifurcation of periodic orbits (the curve T_2), followed by the breakdown of a 2-torus;
- Saddle-node bifurcation of periodic orbits taking place on a strange attractor (the curve SP_4), the so-called intermittency route [30].

Similar routes have been described in many studies of low-order atmospheric models [31,11,32–34]. We here establish a new link

between intermittency due to nonlinear instability of waves and low-frequency variability.

An outline of the rest of the paper is now given. Section 2 presents the derivation of the low-order model from the 2-layer shallow-water equations. The bifurcation diagram of the low-order model is discussed in Section 3.1, followed by analysis of the routes to chaos in Section 3.2. Section 3.3 explains the model phenomenology in terms of mathematical concepts (bifurcations, intermittency) and Section 3.4 provides physical interpretation. Finally, in Section 4 our results are discussed in the context of the existing scientific literature.

2. Model

We consider atmospheric flow in two layers. In each layer the velocity field (u, v) is 2-dimensional. The thickness h of each layer is variable, which is the only 3-dimensional aspect of this model. The governing equations are given by a system of six partial differential equations. By means of truncated Fourier expansions and a Galerkin projection we obtain a low-order model which consists of a 46-dimensional system of ordinary differential equations.

2.1. The 2-layer shallow-water equations

The constants H_1 and H_2 denote the mean thickness of each layer, and the fields η'_1 and η'_2 denote deviations from the mean thickness, where primes indicate that the variable is dimensional. The thickness fields of the two layers are given by

$$h'_1 = H_1 + \eta'_1 - \eta'_2, \tag{1}$$

$$h'_2 = H_2 + \eta'_2 - h'_b, \tag{2}$$

where h_b denotes the bottom topography profile; see Fig. 2. The pressure fields are related to the thickness fields by means of the hydrostatic relation

$$p'_1 = \rho_1 g(h'_1 + h'_2 + h'_b), \tag{3}$$

$$p'_2 = \rho_1 g h'_1 + \rho_2 g(h'_2 + h'_b), \tag{4}$$

where the constants ρ_1 and ρ_2 denote the density of each layer.

The governing equations are nondimensionalised using scales L, U, L/U, D, and $\rho_0 U^2$ for length, velocity, time, depth, and pressure, respectively, and are given by

$$\frac{\partial u_\ell}{\partial t} + u_\ell \frac{\partial u_\ell}{\partial x} + v_\ell \frac{\partial u_\ell}{\partial y} = -\frac{\partial p_\ell}{\partial x} + (Ro^{-1} + \beta y)v_\ell$$
$$- \sigma\mu(u_\ell - u_\ell^*) + Ro^{-1}E_H \Delta u_\ell - \sigma r \delta_{\ell,2} u_\ell$$

$$\frac{\partial v_\ell}{\partial t} + u_\ell \frac{\partial v_\ell}{\partial x} + v_\ell \frac{\partial v_\ell}{\partial y} = -\frac{\partial p_\ell}{\partial y} - (Ro^{-1} + \beta y)u_\ell \tag{5}$$
$$- \sigma\mu(v_\ell - v_\ell^*) + Ro^{-1}E_H \Delta v_\ell - \sigma r \delta_{\ell,2} v_\ell$$

$$\frac{\partial h_\ell}{\partial t} + u_\ell \frac{\partial h_\ell}{\partial x} + v_\ell \frac{\partial h_\ell}{\partial y} = -h_\ell \left(\frac{\partial u_\ell}{\partial x} + \frac{\partial v_\ell}{\partial y} \right)$$
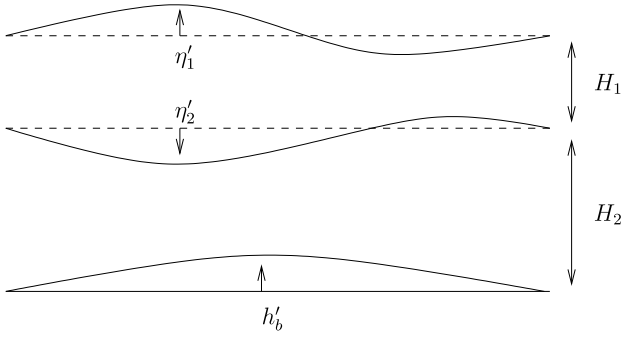
Fig. 2. Layers in the shallow-water model.

where u_ℓ and v_ℓ are eastward and northward components of the 2-dimensional velocity field, respectively. In addition, the nondimensional pressure terms are given by

$$p_1 = \frac{\rho_1}{\rho_0} F(h_1 + h_2 + h_b),$$

$$p_2 = \frac{\rho_1}{\rho_0} Fh_1 + \frac{\rho_2}{\rho_0} F(h_2 + h_b).$$

Several nondimensional numbers appear in the governing equations: the advective time scale σ, the nondimensional β-parameter, the Rossby number Ro, the horizontal Ekman number E_H, and the inverse Froude number F. These parameters have the following expressions in terms of the dimensional parameters:

$$\sigma = \frac{L}{U}, \qquad \beta = \frac{\beta_0 L^2}{U}, \qquad Ro = \frac{U}{f_0 L},$$

$$E_H = \frac{A_H}{f_0 L^2}, \qquad F = \frac{gD}{U^2}.$$

Standard values of the dimensional parameters are listed in Table 2.

The dynamical equations will be considered on the zonal β-plane channel

$$0 \le x \le L_x/L, \qquad 0 \le y \le L_y/L.$$

Suitable boundary conditions have to be imposed: we require all fields to be periodic in the x-direction. At $y = 0, L_y/L$ we impose the conditions

$$\frac{\partial u_\ell}{\partial y} = \frac{\partial h_\ell}{\partial y} = v_\ell = 0.$$

The model is forced by relaxation to an apparent westerly wind given by the profile

$$u_1^*(x, y) = \alpha_1 U_0 U^{-1}(1 - \cos(2\pi yL/L_y)), \qquad v_1^*(x, y) = 0,$$

$$u_2^*(x, y) = \alpha_2 U_0 U^{-1}(1 - \cos(2\pi yL/L_y)), \qquad v_2^*(x, y) = 0,$$

where the dimensional parameter U_0 controls the strength of the forcing and the nondimensional parameters α_1 and α_2 (Table 2) control the vertical shear of the forcing. For the bottom topography we choose a profile with zonal wave number 3:

$$h_b(x, y) = h_0 D^{-1}(1 + \cos(6\pi xL/L_x)),$$

where the dimensional parameter h_0 controls the amplitude of the topography. We require that the bottom topography is contained entirely in the bottom layer which implies the restriction $h_0 \le H_2/2$.

2.2. The low-order model

The governing equations in (5) form a dynamical system with an infinite-dimensional state space. We reduce the infinite-dimensional system to a system of finitely many ordinary differential equations by means of a Galerkin projection. This amounts to an expansion of the unknown fields u_ℓ, v_ℓ, h_ℓ in terms of known basis functions, depending only on spatial variables,

with unknown coefficients, depending only on time. An orthogonal projection onto the space spanned by the basis functions gives a set of finitely many ordinary differential equations for the expansion coefficients.

As basis functions we will use the Fourier modes with half wavenumbers. For an integer $k \ge 0$ and a real number $\alpha > 0$ these functions are given by

$$c_k(\xi; \alpha) := \begin{cases} \dfrac{1}{\sqrt{\alpha}} & k = 0 \\[2mm] \sqrt{\dfrac{2}{\alpha}} \cos\left(\dfrac{k\pi\xi}{\alpha}\right) & k > 0, \end{cases} \tag{6}$$

$$s_k(\xi; \alpha) := \sqrt{\frac{2}{\alpha}} \sin\left(\frac{k\pi\xi}{\alpha}\right),$$

where $\xi \in [0, \alpha]$, and the numerical factors serve as normalisation constants.

Deciding which Fourier modes to retain in the Galerkin projection is a non-trivial problem. A priori it is not known which choice captures the dynamics of the infinite-dimensional system in the best possible way. In [35–37] this problem has been addressed in the setting of a Rayleigh–Bénard convection problem by checking qualitative changes in dynamical behaviour and quantitative information on the location of branches of equilibria and their bifurcations, while increasing the number of retained modes. In our paper we choose a different approach: first of all, we construct a minimal model, retaining only those Fourier modes which are essential to reproduce atmospheric low-frequency behaviour. Observational evidence (see the Introduction) suggests that the fundamental physical processes involved in low-frequency behaviour manifest themselves at zonal wavenumbers less than 5 [19]. For the above reasons, we choose wavenumbers $m = 0, 3$ in the zonal direction, and the wavenumbers $n = 0, 1, 2$ in the meridional direction. Let

$$R = \{(0, 0), (0, 1), (0, 2), (3, 0), (3, 1), (3, 2)\}$$

denote the set of retained wave number pairs. Moreover, set $a = L_x/L$ and $b = L_y/L$. Then all nondimensional fields are expanded as

$$\begin{aligned} u_\ell(x, y, t) = \sum_{(m,n) \in R} [\widehat{u}^c_{\ell,m,n}(t) c_{2m}(x; a) \\ + \widehat{u}^s_{\ell,m,n}(t) s_{2m}(x; a)] c_n(y; b), \end{aligned}$$

$$v_\ell(x, y, t) = \sum_{(m,n) \in R} [\widehat{v}^c_{\ell,m,n}(t) c_{2m}(x; a) + \widehat{v}^s_{\ell,m,n}(t) s_{2m}(x; a)] s_n(y; b),$$

$$\begin{aligned} h_\ell(x, y, t) = \sum_{(m,n) \in R} [\widehat{h}^c_{\ell,m,n}(t) c_{2m}(x; a) \\ + \widehat{h}^s_{\ell,m,n}(t) s_{2m}(x; a)] c_n(y; b). \end{aligned}$$

In this way the truncated expansions satisfy the boundary conditions.

By substituting the truncated expansions in (5) and projecting (with respect to the standard inner product) the governing equations on the Fourier modes, we obtain a system of ordinary differential equations for the time-dependent Fourier coefficients. With the above choice of the retained wavenumbers, we need 9, 6, and 9 coefficients for the fields u_ℓ, v_ℓ, and h_ℓ, respectively. However, due to conservation of mass, it turns out that the coefficients $\widehat{h}_{\ell,0,0}$ are constant in time and therefore they can be treated as a constant. Hence, the low-order model is 46-dimensional. Formulas to compute the coefficients of the low-order model are presented in Appendix B.

3. Results

We here investigate the dynamics of the low-order model, starting from a description of the bifurcations in Fig. 1 (Section 3.1). It is shown how low-frequency dynamical behaviour is linked

Table 2
Standard values of the fixed parameters.

Parameter	Meaning	Value	Unit
A_H	Momentum diffusion coefficient	1.0×10^2	$m^2 \, s^{-1}$
μ	Relaxation coefficient	1.0×10^{-6}	s^{-1}
r	Linear friction coefficient	1.0×10^{-6}	s^{-1}
f_0	Coriolis parameter	1.0×10^{-4}	s^{-1}
β_0	Planetary vorticity gradient	1.6×10^{-11}	$m^{-1} \, s^{-1}$
ρ_0	Reference density	1.0	$kg \, m^{-3}$
ρ_1	Density (top layer)	1.01	$kg \, m^{-3}$
ρ_2	Density (bottom layer)	1.05	$kg \, m^{-3}$
g	Gravitational acceleration	9.8	$m \, s^{-2}$
α_1	Zonal velocity forcing strength (top layer)	1.0	
α_2	Zonal velocity forcing strength (bottom layer)	0.5	
L_x	Channel length	2.9×10^7	m
L_y	Channel width	2.5×10^6	m
H_1	Mean thickness (top layer)	5.0×10^3	m
H_2	Mean thickness (bottom layer)	5.0×10^3	m
L	Characteristic length scale	1.0×10^6	m
U	Characteristic velocity scale	1.0×10^1	m/s
D	Characteristic depth scale	1.0×10^3	m

to strange attractors, which occur in a relatively large parameter domain. The onset of chaotic dynamics is explained in terms of bifurcation scenarios ("routes to chaos", Section 3.2). Lastly, physical interpretation of the dynamics is given in terms of atmospheric low-frequency variability (Section 3.4).

3.1. Organisation of the parameter plane

In this section we give a detailed description of the bifurcation diagram and we explain how this clarifies various parts of the Lyapunov diagram. The bifurcations detected in our model are standard, and they are discussed in detail in, e.g., [38].

Lyapunov diagram

The top panel of Fig. 1 contains the Lyapunov diagram of the attractors of the low-order model. This is produced by scanning the (U_0, h_0)-parameter plane from left to right and classifying the detected attractor by means of Lyapunov exponents, see Appendix A and [39,40] for details. Along each line of constant h_0 we start with a fixed initial condition when $U_0 = 12$ m/s. For the next parameter values on this line we take the last point of the previous attractor as an initial condition for the next one.

We do not exclude the possibility of coexisting attractors, but this cannot be detected by our procedure. By means of more refined procedures, with varying initial conditions, coexistence of attractors can be detected as well. For large values of the parameter U_0 orbits can escape to infinity (see the white parts in Fig. 1), but this also depends on the chosen initial condition. These unbounded orbits have also been detected in [41].

Bifurcations of equilibria

The transition from stationary to periodic behaviour in the Lyapunov diagram (Fig. 1) is explained by Hopf bifurcations where an equilibrium loses stability. Bifurcations are computed here with the AUTO–07p software [42], see Appendix A. A stable equilibrium is found for $U_0 = 0$ m/s and remains stable up to $U_0 = 12.2$ m/s. The equilibrium undergoes one or more Hopf bifurcations for $U_0 > 12.2$ m/s approximately: loss of stability occurs at curves H_1 and H_2 in Fig. 1 (we only focus on bifurcations leading to loss of stability here). Periodic orbits born at the H_1 curve have periods of about 10 days, whereas periodic orbits born at the H_2 curve have periods in the range of 30–60 days; see Figs. 3 and 4, respectively.[1]

A pair of degenerate Hopf points occur at the tangencies between the Hopf curves $H_{1,2}$ and the curves SP_1 and SP_2 of saddle-node bifurcations of periodic orbits. The bifurcation type on $H_{1,2}$ changes from supercritical to subcritical at the degenerate Hopf points. Two branches of stable periodic orbits are thus formed on either of $SP_{1,2}$ or $H_{1,2}$.

Two curves SN_1 and SN_2 of saddle-node bifurcations of equilibria meet in a cusp. This leads to a domain in the parameter plane for which three equilibria coexist. The boundaries of this domain are tangent to the Hopf curves H_1 and H_2 at three different Hopf-saddle-node bifurcation points. Moreover, a Bogdanov–Takens point occurs along one of the saddle-node curves, where one additional real eigenvalue crosses the imaginary axis.

Bifurcations of periodic orbits born at H_1 or SP_1

The periodic orbits born at the curves H_1 or SP_1 lose stability through either Hopf–Neĭmark–Sacker or saddle-node bifurcations. The Hopf–Neĭmark–Sacker curve T_1 originates from a Hopf–Hopf point at the curve H_1, where two pairs of complex eigenvalues cross the imaginary axis. The saddle-node curves $SP_{3,4}$ are joined in a cusp, and the curve SP_4 forms part of a boundary between periodic and chaotic behaviour in the Lyapunov diagram. Moreover, the curve SP_4 becomes tangent to the Hopf–Neĭmark–Sacker curve T_1 at a Hopf-saddle-node bifurcation point of periodic orbits.

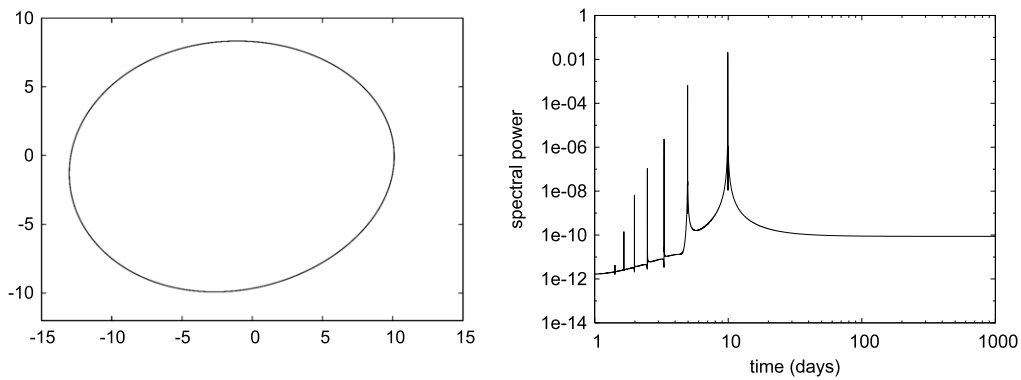*Bifurcations of periodic orbits born at H_2 or SP_2*

The periodic orbits born at the curves H_2 or SP_2 may lose stability through either a period doubling bifurcation or Hopf–Neĭmark–Sacker bifurcations. The former occurs on curve P_1, which is the first of a cascade leading to a chaotic attractor, see the next section. Hopf–Neĭmark–Sacker bifurcations occur on curves T_2 and T_3 in Fig. 1: T_2 originates from a Hopf-saddle-node bifurcation point of periodic orbits, and T_3 is tangent to the period doubling curve P_1 at a 1:2 resonance point.

3.2. Routes to chaos

We have identified three different routes from orderly to chaotic behaviour. All of them involve one or more bifurcations of the stable periodic orbits described in the previous section.

Period doublings

The periodic orbits born at the Hopf bifurcation H_2 lose stability through a period doubling bifurcation (see previous section). Three period doubling curves $P_{1,2,3}$ are shown in Fig. 1, and we expect that they are the first of an infinite cascade. Indeed, a magnification of the Lyapunov diagram (Fig. 5) reveals a large

---

[1] Unless specified otherwise, attractors are plotted on directions of maximal amplitude. See Appendix A.3 for details. Since the projection is computed numerically, labels for the axes are omitted.

Fig. 3. Periodic orbit born at Hopf bifurcation H_1 ($U_0 = 13.32$ m/s, $h_0 = 800$ m) and its power spectrum. The period is approximately 10 days.
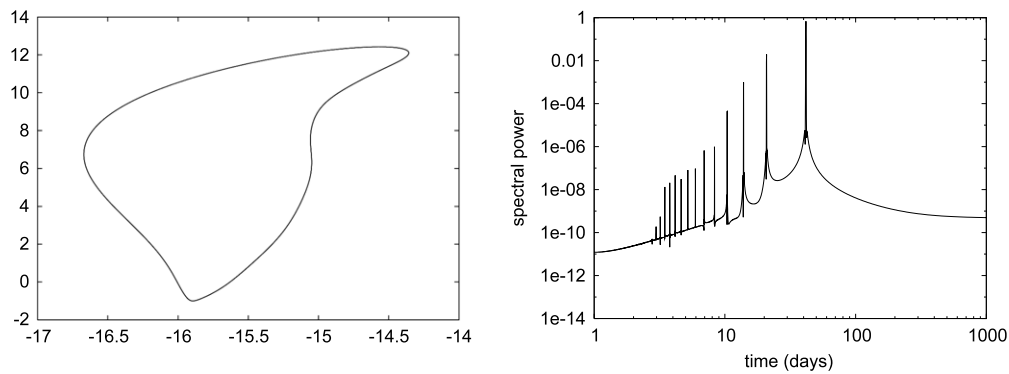
Fig. 4. Periodic orbit born at Hopf bifurcation H_2 ($U_0 = 14.64$ m/s, $h_0 = 1400$ m) and its power spectrum. The period is approximately 60 days.
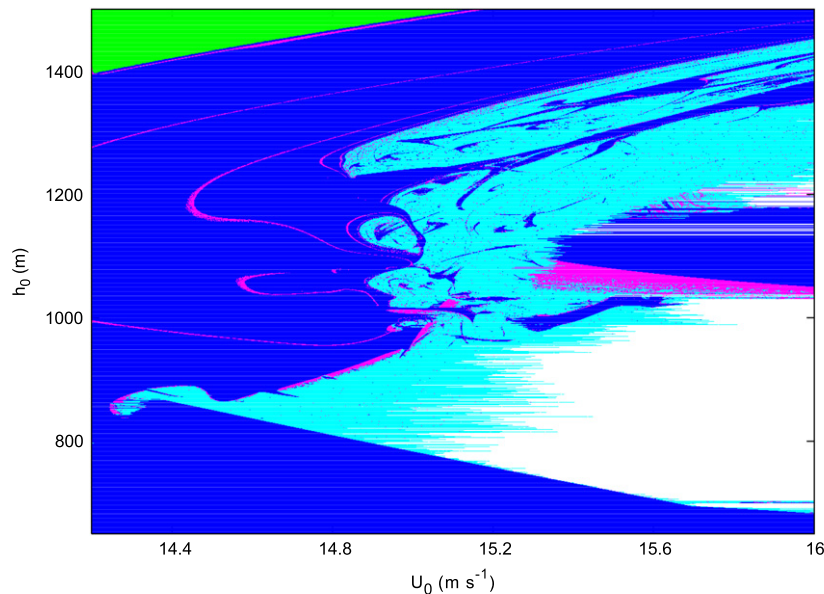
Fig. 5. Magnification of the Lyapunov diagram in Fig. 1; see Table 1 for the colour coding. (For interpretation of the references to colour in this figure legend, the reader is referred to the web version of this article.)

chaotic region at the right of P_3, interrupted by narrow domains of periodic behaviour. Occurrence of these windows of periodicity is confirmed in the diagrams in Fig. 6. However, these gaps disappear for lower values of the parameter h_0, and chaotic behaviour seems to be persistent on a continuum.

Fig. 7 shows a twice-doubled stable periodic orbit along the cascade and a strange attractor after the end of the cascade. The dynamics on the strange attractor exhibits low-frequency behaviour in the range 20–200 days (see the power spectrum in Fig. 7). The peaks around 100 and 200 days are 'inherited' from the twice-doubled periodic orbit. In turn, these originate from the same branch of periodic orbits as in Fig. 4: just before the first period doubling bifurcation P_1 ($U_0 = 13.9$ m/s, $h_0 = 1200$ m) this stable periodic orbit has a period of approximately 50 days (not shown).

Broken torus

2-torus attractors occur in a narrow region separating periodic from chaotic behaviour in the Lyapunov diagram (Fig. 5).
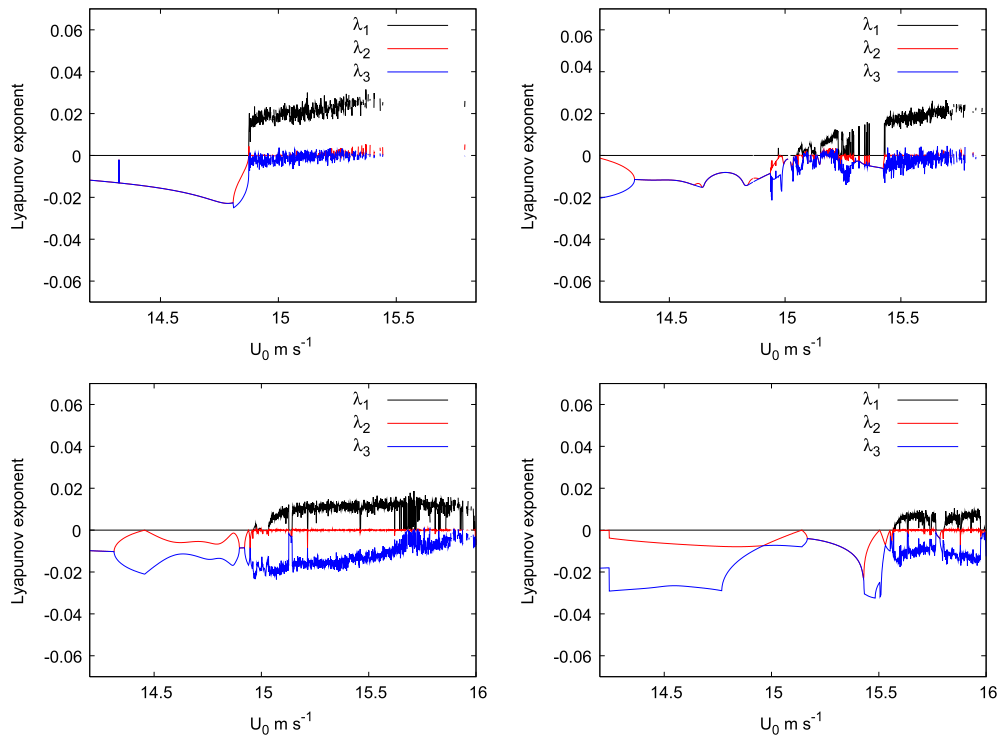
Fig. 6. The three largest Lyapunov exponents $\lambda_1 \geq \lambda_2 \geq \lambda_3$ (nondimensional) as a function of U_0. The value of the parameter h_0 is fixed at $h_0 = 800$ m (top left), $h_0 = 1000$ m (top right), $h_0 = 1200$ m (bottom left), and $h_0 = 1400$ m (bottom right).
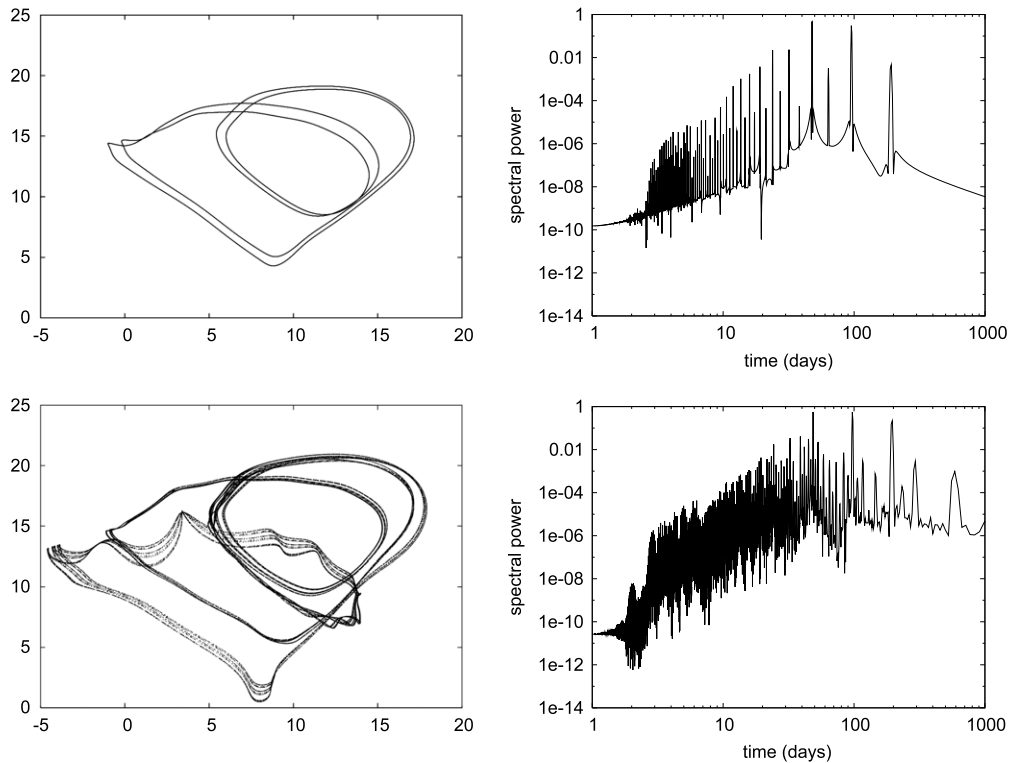
Fig. 7. Attractors (left panels, same projection) and their power spectra (right) for $h_0 = 1200$ m. Top: periodic orbit after two period doublings ($U_0 = 14.48$ m/s). Bottom: strange attractor after a period doubling cascade ($U_0 = 15$ m/s).

The 2-torus attractors branch off from periodic orbits at the Hopf–Neĭmark–Sacker bifurcations on curve T_2. The periodic orbits losing stability here belong to the branch created at the Hopf curve H_2 (see previous section). The 2-torus attractors quickly break down giving rise to a strange attractor (Fig. 8). This

strange attractor exhibits low-frequency behaviour in the range 10–100 days. The main spectral peaks at 56 and 11 days are inherited from the 2-torus, which has two frequencies $\omega_1 = 0.0178$ days^{-1} and $\omega_2 = 0.0888$ days^{-1} for parameters right after the Hopf–Neĭmark–Sacker bifurcation. In turn the torus inherits
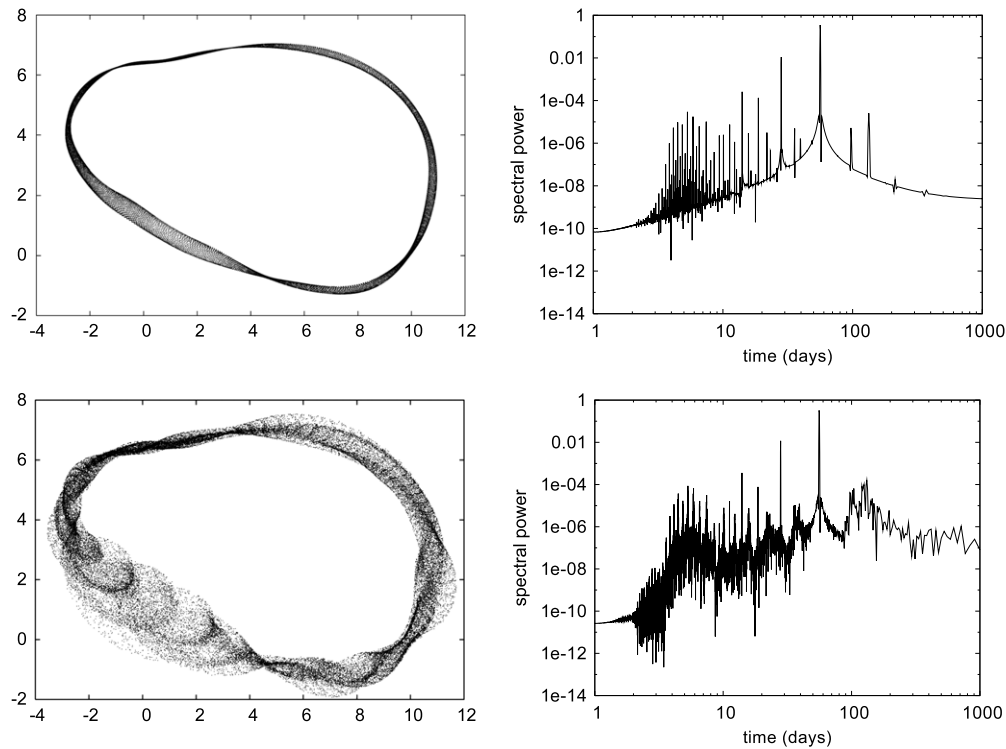
Fig. 8. Same as Fig. 7 for $h_0 = 900$ m: a 2-torus attractor (top, $U_0 = 14.75$ m/s) and a strange attractor after the 2-torus breakdown (bottom, $U_0 = 14.78$ m/s).

one of the frequencies from the periodic orbit, which has a period of approximately 56 days just before the Hopf–Neĭmark–Sacker bifurcation ($U_0 = 14.74$ m/s, $h_0 = 900$ m, not shown).

The process leading to the creation of the above strange attractor involves transition through a number of phase-locking windows as U_0 is increased. Fig. 9 shows Poincaré sections for $U_0 = 14.750$ m/s up to $U_0 = 14.780$ m/s with step 0.001 m/s with $h_0 = 900$ m fixed. Densely filled invariant circles and periodic points in the Poincaré section correspond to quasi-periodic 2-tori and periodic orbits of the flow, respectively. Periodicity windows with periods 16, 25, 34, 9, and 11 are crossed as U_0 is increased, until the invariant circle breaks up and the quasi-periodic dynamics is replaced by chaotic dynamics. The size of the attractor is growing rapidly in phase space as U_0 is changed. The breakdown of a 2-torus often involves homo- and heteroclinic bifurcations; see Section 3.3 for details.

Intermittency

The saddle-node curve SP_4 in Fig. 1 forms one of the boundaries between the regions of periodic and chaotic behaviour in the Lyapunov diagram. Fig. 10 (top left panel) shows a stable periodic orbit born at the curve SP_1; the period is 10 days. When the parameters cross the saddle-node curve SP_4, the stable periodic disappears and a strange attractor is found; see Fig. 10 (bottom left panel).

The dynamics on the attractor seems to consist of a sequence of passages close to heteroclinic orbits between different objects. The attractor coexists with (at least) the following objects.

- An unstable periodic orbit with a 2-dimensional unstable manifold (due to one pair of complex conjugate Floquet multipliers in the right half plane).
- Three unstable equilibria with unstable manifolds of dimension 4, 3, and 2 (due to two, one, and one pair(s) of complex conjugate eigenvalues in the right half plane, respectively).

Fig. 11 shows that the dynamics on the attractor consists of different regimes.

- Regimes of nearly regular periodic behaviour correspond to intermittency near the formerly existing stable periodic orbit, which disappeared through the saddle-node curve SP_4.
- Regimes of nearly stationary behaviour are observed when the orbit approaches one of the three equilibria mentioned above.
- The previous two regimes are alternated with irregular behaviour.

The intermittency regimes often occur directly after the orbit approached one the equilibria, but this is not always the same equilibrium. We have tested this by computing a large number of orbits, for which the initial conditions are random points in the tangent space to the unstable manifold of the equilibrium. The intermittency regime can be reached immediately by starting near the equilibria with the 4-dimensional and 3-dimensional unstable manifolds. When starting near the equilibrium with the 2-dimensional unstable manifold, however, the orbit shows irregular behaviour before reaching the intermittency regime.

Orbits on the attractor never approach the unstable periodic orbit within a small distance. Again we have computed a large number of orbits, for which the initial conditions are random points in the tangent space of the unstable manifold of the periodic orbit. In general, first a long transient of irregular behaviour is observed, and then the orbit reaches the intermittency regime.

3.3. Theoretical remarks

The results of the previous subsections are now interpreted in terms of known theory.

Bifurcations of equilibria and periodic orbits

The codimension-1 bifurcations of equilibria and periodic orbits we have found are standard and have been described extensively in the literature; see, for instance, [43–45,38] and the references therein. For each bifurcation a (truncated) normal form can be derived by restricting the vector field to an approximation of a centre manifold. This normal form can be used to check the
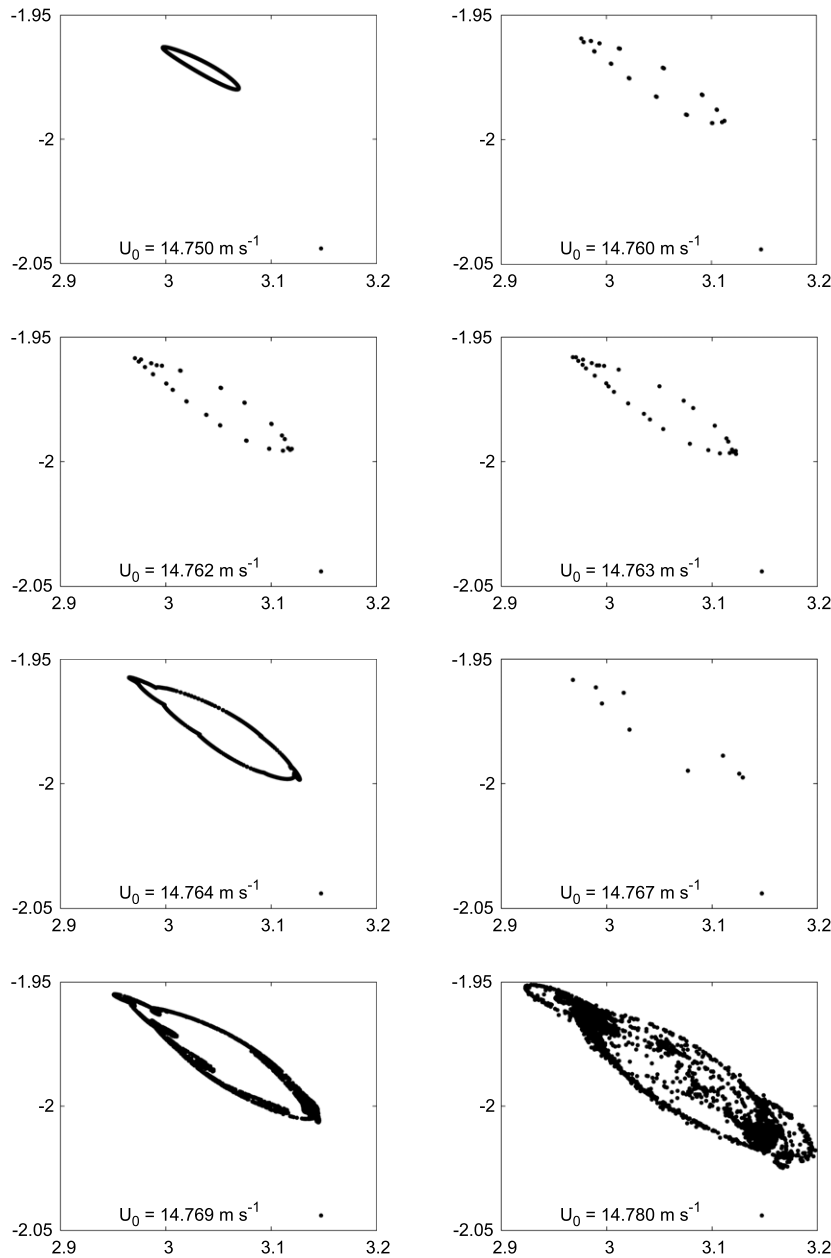
Fig. 9. Breakdown of the 2-torus attractor, visualised in the Poincaré section $\widehat{u}_{2,0,0} = 1.8$, projection on $(\widehat{u}_{2,0,1}, \widehat{u}_{2,0,2})$: alternation of periodic, quasi-periodic, and chaotic dynamics as the parameter U_0 is varied with constant $h_0 = 900$ m.

appropriate genericity and transversality conditions and to study different unfolding scenarios. This methodology is described in detail in [38], see [46] for other methods of computing normal forms.

The codimension-2 bifurcations of equilibria (Bogdanov–Takens, Hopf–Hopf, and Hopf-saddle-node) have been described in detail in [38]. In this case, however, the truncated normal forms only provide partial information on the dynamics near the bifurcation. The Hopf-saddle-node bifurcation for diffeomorphisms has been studied extensively in [39,40].

Period doubling route

This scenario for the birth of strange attractors is theoretically well-understood, see for example [47,48] and references therein. Strange attractors obtained from infinite period doublings in one direction may be reached at once by homo- and heteroclinic tangencies from another direction [49]. When curves of period doubling bifurcations form unnested islands, the chaotic region can be reached by a variety of routes, including the breakdown of a 2-torus or the sudden appearance of a chaotic attractor [50].

2-tori and their breakdown

It is well known that 2-torus attractors of dissipative systems generically occur as families of quasi-periodic attractors parameterised over a Cantor set (of positive 1-dimensional Hausdorff measure) in a Whitney-smooth way, see [43,51,44]. These attractors are often a transient stage between periodic and chaotic dynamics.

The birth and death of periodic orbits on an invariant torus occur when the parameters move across Arnol'd resonance tongues. These are regions in the parameter plane bounded by pairs of curves of saddle-node bifurcations originating from a common resonant Hopf–Neĭmark–Sacker bifurcation. For parameters inside a tongue the dynamics on the torus is phase locked, meaning that the invariant circle of the Poincaré map (defined by a section transversal to the torus) is the union of a stable periodic point and the unstable manifolds of an unstable periodic point (see, for example,
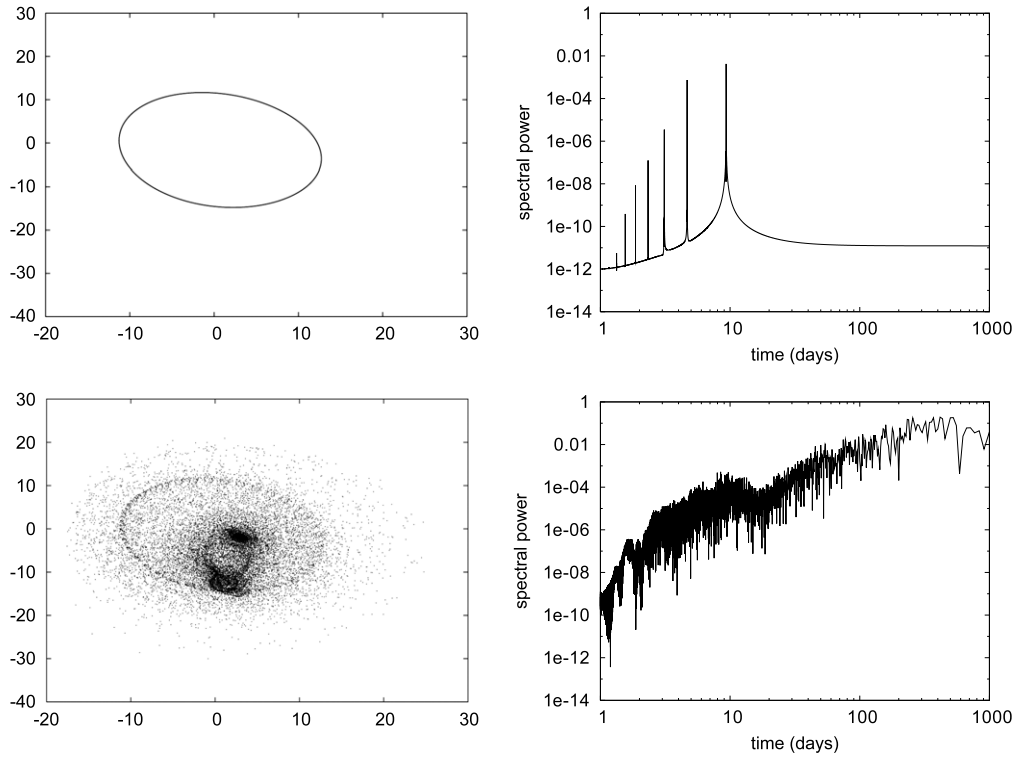
Fig. 10. Same as Fig. 7 for $h_0 = 800$ m. Top row: stable periodic orbit before the saddle-node bifurcation ($U_0 = 14.87$ m/s). Bottom row: strange attractor after the saddle-node bifurcation ($U_0 = 15$ m/s).
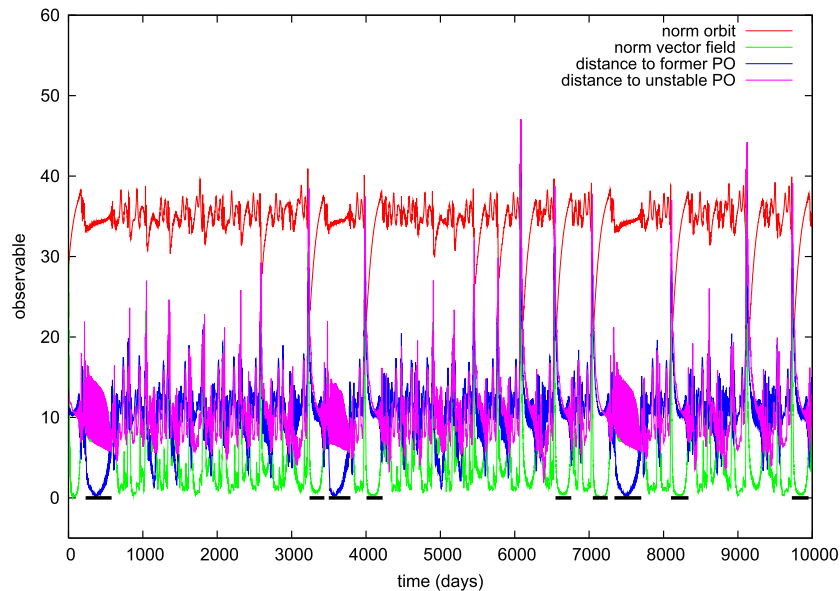
Fig. 11. Four time series, derived from one orbit on the attractor in Fig. 10 using four different observables: norm of the orbit (red), norm of the vector field along the orbit (green), distance of the orbit to the position of the formerly existing periodic orbit (blue), and distance to the unstable periodic orbit (magenta). Black bars underneath mark time intervals of intermittency near either the periodic orbit or an equilibrium. (For interpretation of the references to colour in this figure legend, the reader is referred to the web version of this article.)

the top right panel in Fig. 9). The circle can be destroyed by homoclinic tangencies between the stable and unstable manifolds of the unstable periodic point, or the circle can interact with other objects via heteroclinic tangencies. See [52,47] for an extensive discussion.

Intermittency

The phenomenon of intermittency near a saddle-node bifurcations is well known, but it only explains a part of the dynamics on the strange attractor in Fig. 10. Furthermore, the geometrical

structure of the strange attractor remains unclear. In many systems, strange attractors are formed by the closure of the unstable manifold of a saddle-like object. This *Ansatz* is discussed in several works, see e.g. [47,44] and references therein. However, the structure of the attractor in Fig. 10 seems to be more complicated, involving interaction with several nearby invariant objects (equilibria, periodic orbits) of saddle type.

We consider it as an interesting problem for future research to investigate the structure of the attractor in Fig. 10 in more detail.
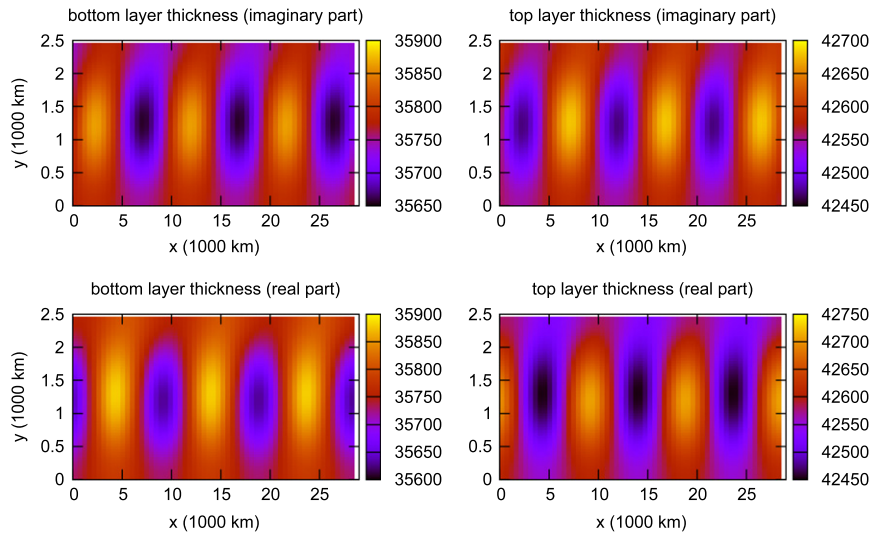
Fig. 12. Patterns of layer thickness associated with the eigenvectors at the Hopf bifurcation H_1, for $U_0 = 12.47$ m/s and $h_0 = 800$ m. The scale is arbitrary, since any scalar multiple of (7) is a solution of the linearised vector field.
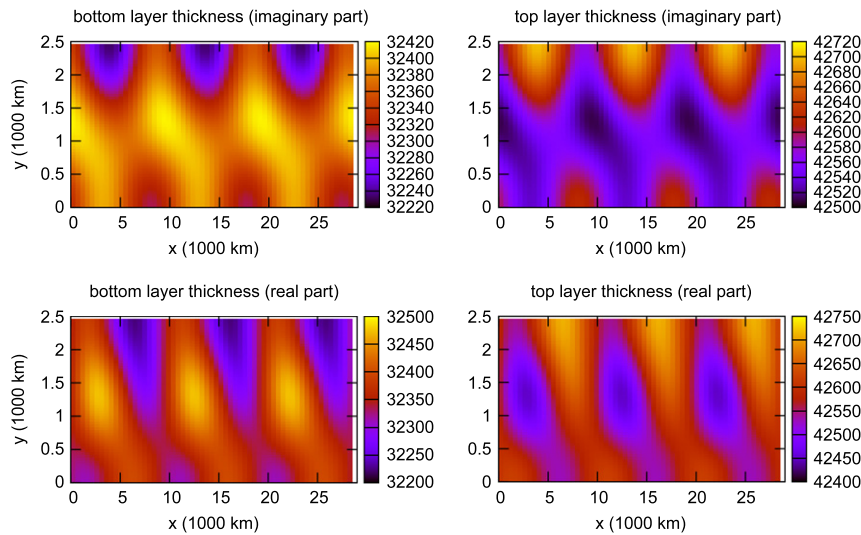
Fig. 13. Same as Fig. 12 at Hopf curve H_2, for $U_0 = 13.31$ m/s and $h_0 = 1200$ m.

At least the stable and unstable manifolds of the equilibria and the periodic orbit should be computed, in order to gain more insight in the structure of the attractor. Next, the 'genealogy' of the attractor should be determined, e.g., by identifying whether the present shape is created through a sequence of bifurcations. For a more thorough analysis it might be necessary to derive a simpler model for this attractor, having a state space with the lowest possible dimension.

3.4. Physical interpretation

In this section we investigate the physical aspects (mainly instability and wave propagation) associated with the attractors analysed in the previous section. Hopf bifurcations are first interpreted in terms of geophysical fluid dynamical instabilities, giving rise to planetary waves. The structure of these waves is then studied through Hovmöller diagrams of the vorticity field [53]. This allows us to visualise structural differences and changes, such as the onset of large-scale meanders in the westerly wind.

Hopf bifurcations

A fluid is said to be hydrodynamically unstable when small perturbations of the flow can grow spontaneously, drawing energy

from the mean flow. At a Hopf bifurcation an equilibrium loses its stability and gives birth to a periodic orbit. In the context of a fluid this can be interpreted as a steady flow becoming unstable to an oscillatory perturbation (such as a travelling wave). Two wave instabilities are well known in geophysical fluid dynamics: barotropic and baroclinic instabilities. The fundamental difference lies in the source of energy: perturbations derive their energy from the horizontal shear of the mean flow in a barotropically unstable flow. In a baroclinically unstable flow, perturbations derive their kinetic energy from the potential energy of the mean flow associated with the existence of vertical shear in the velocity field. The reader is referred to standard textbooks on geophysical fluid dynamics for a full discussion on this subject [54–56].

At a Hopf bifurcation the Jacobian matrix of the vector field has two eigenvalues $\pm \omega i$ on the imaginary axis. Let $\Phi_1 \pm i\Phi_2$ denote corresponding eigenvectors, then

$$P(t) = \cos(\omega t)\, \Phi_1 - \sin(\omega t)\, \Phi_2 \qquad (7)$$

is a periodic orbit of the vector field obtained by linearisation around the equilibrium undergoing the Hopf bifurcation. This can be interpreted as a wave-like response to a perturbation of the equilibrium. The propagation of the physical pattern associated to
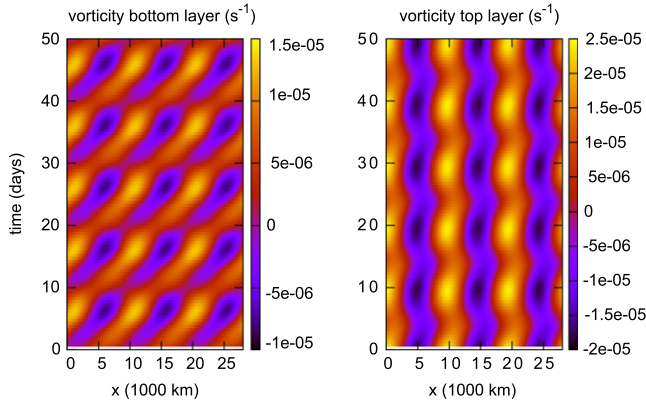
Fig. 14. Hovmöller diagram of the periodic orbit of Fig. 3. The magnitude of the vorticity field is plotted as a function of time and longitude while keeping the latitude fixed at $y = 1250$ km. Observe the eastward propagation in the bottom layer.
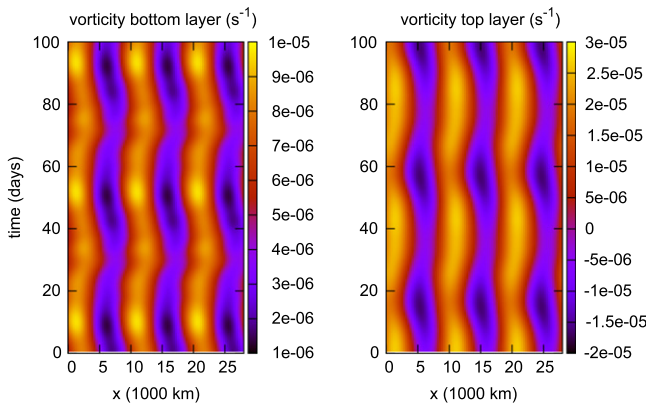
Fig. 15. Same as Fig. 14 for the periodic orbit of Fig. 4. Observe that this wave is non-propagating in both layers.

this wave can be followed by looking at the physical fields at the phases $P(-\pi/2\omega) = \Phi_2$ and $P(0) = \Phi_1$. Fig. 12 shows the layer thickness associated with the eigenvectors at the Hopf bifurcation H_1. Clearly, positive and negative anomalies are opposite in each layer. Moreover, this is accompanied by vertical shear in the velocity fields (not shown in the figure). Hence, we interpret this Hopf bifurcation as a mixed barotropic/baroclinic instability. The same plot for the Hopf bifurcation H_2 is given in Fig. 13. Here, we see again that positive and negative anomalies are opposite in each layer. Therefore, we interpret this Hopf bifurcation also as a mixed barotropic/baroclinic instability.
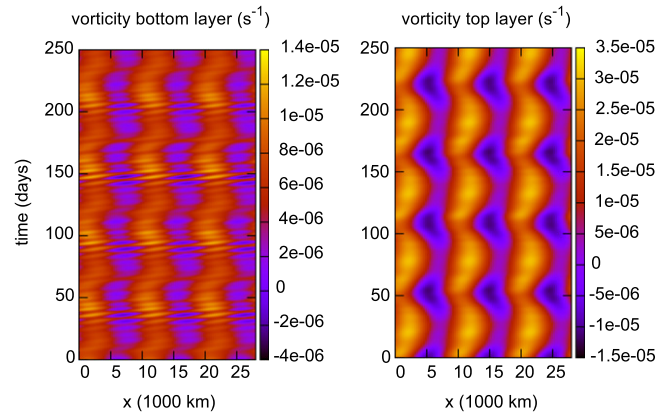
The periodic orbits

The physical patterns associated with periodic dynamics change with the parameters U_0 and h_0. Namely the propagation features of the periodic orbits in Figs. 3 and 4 differ from those at the Hopf bifurcations that gave birth to these orbits. The vorticity field associated with the periodic orbit in Fig. 3 propagates eastward in the bottom layer, whereas it does not propagate in the top layer, see the Hovmöller diagram in Fig. 14. Also, the variability is stronger in the top layer. The vorticity field associated with the periodic orbit in Fig. 4 is non-propagating in both layers (Fig. 15).

Period doublings

The strange attractor after the period doubling sequence is associated with non-propagating wave behaviour in both layers (Fig. 16). The characteristic time scale is approximately 100 days. Again the variability is stronger in the upper layer.
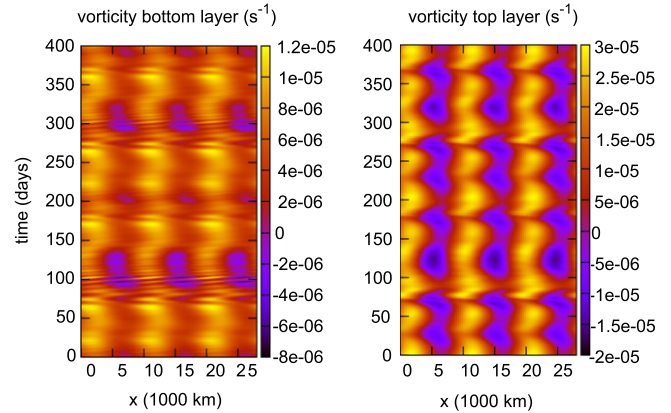
Fig. 16. Same as Fig. 14 for the strange attractor of Fig. 7. The non-propagating nature is inherited from the periodic orbit of Fig. 3. Observe the irregular variability in the bottom layer. This is due to the harmonics induced by the period doubling bifurcations.

Fig. 17. Same as Fig. 14 for the strange attractor of Fig. 8. Again, the non-propagating nature is inherited from the periodic orbit of Fig. 3. The two fundamental frequencies (11 and 56 days) of the formerly existing 2-torus can still be identified.

Broken torus

The dynamics on the broken 2-torus attractor corresponds to non-propagating wave behaviour in both layers (Fig. 17). The dominant time scale in the top layer (approximately 50 days) is longer than in the bottom layer (5 to 10 days). Both time scales are represented by peaks in the power spectrum (Fig. 8).

Intermittency

The strange attractor in Fig. 10 is characterised by intermittent transitions between long time episodes of nearly stationary behaviour and episodes with eastward propagating waves in the bottom layer and non-propagating waves in the top layer, see Fig. 18.

4. Discussion and conclusions

The results of our investigation are consistent with the following hypothesis: that one of the basic physical processes underlying low-frequency atmospheric variability in the Northern Hemisphere consists of irregular planetary scale waves with non-propagating and temporally persistent character. Such waves are associated to mixed baroclinic/barotropic instabilities, where the baroclinic character is non-standard and a fundamental role is played by the interaction of the westerly flow with orography. These features agree qualitatively not only with observational evidence, but also with previous theories mainly based on
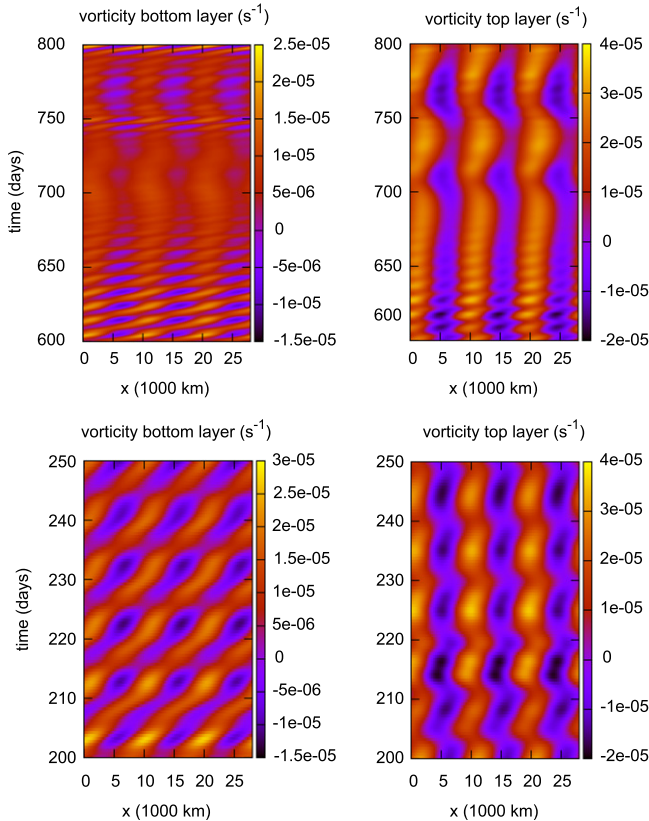
Fig. 18. Hovmöller diagrams of the strange attractor of Fig. 10 for two different time intervals. The magnitude of the vorticity field is plotted as a function of time and longitude while keeping the latitude fixed at $y = 1250$ km. The lower panels correspond to the intermittency regime near the vanished periodic orbit. The propagating nature in the bottom layer is inherited from the periodic orbit of Fig. 4. The top panels are associated with a stationary regime, where the orbit approaches one of the nearby equilibria.

linear instabilities, such as orographic resonance and orographic baroclinic instability [57,9,19,29,23,8,20].

We contribute novel dynamical mechanisms to the on-going discussion on the nature of atmospheric low-frequency variability. Irregularly recurring persistent behaviour is explained in terms of intermittency associated to codimension-1 bifurcations. Specifically, irregular waves arise from two branches of periodic orbits through period doubling cascades, Hopf–Neĭmark–Sacker bifurcations followed by breakdown of a 2-torus attractor, and saddle-node bifurcations taking place on strange attractors (see Fig. 1 and Section 3.2). Dominant time scales and propagation patterns are inherited from the periodic orbits and are in broad quantitative agreement with observational evidence (also see Section 1.2). This intermittent behaviour persists in a large domain of physically relevant parameter values.

Many studies invoking the multiple equilibria approach following Charney and DeVore [10] are based on barotropic models. The dynamics typically involves a Shil'nikov homoclinic bifurcation near a Hopf-saddle-node bifurcation of an equilibrium, see [58] for an overview. We do not take a definite stance on the multiple mode/equilibria versus single mode/equilibrium issue. The approach in this paper is more akin to the spectral analysis ideas of [19,23], see Section 1.1. It has already been proposed that regimes, as identified by modes of probability distribution functions, need not be associated to (metastable) steady states of the dynamical equations [59]. We do not rule out that the intermittency phenomena described in this paper might provide a dynamical mechanisms for the onset of statistical modes unrelated to metastable steady states. This issue deserves specific investigation.

Our modelling approach has major advantages with respect to the barotropic quasi-geostrophic models often used to study low-frequency variability. Orography is a perturbative (small) parameter in quasi-geostrophic theories [28]. Instabilities in barotropic flows are fuelled by the kinetic energy of the flow rather than by the available potential energy [9]. Consequently, the transitions between the quasi-stable equilibria of barotropic models either involve variations of the zonal wind which of the order of 40 m/s (much larger than in reality [57,60]), or occur at low orography (200 m). Our usage of shallow-water models with baroclinic-like forcing has allowed us:

1. to highlight the essential role of orography height in determining the propagating versus non-propagating character of the waves (the latter is only found for orography larger than 850 m);
2. to identify the mixed barotropic/baroclinic character of the waves excited on the zonal flow by the orography.

That our minimal model exhibits temporal variability in the appropriate range is already a non-trivial accomplishment, given the strongly nonlinear nature of the phenomena which we are trying to understand. We believe, however, that a more important achievement is the identification of the underlying physical process, possessing qualitative features in broad agreement with the observational evidence and previous theories. Our admittedly unrealistic "minimal modelling" approach has allowed us to perform an extensive dynamical analysis (see e.g. Fig. 1) offering the useful physical insight enumerated above. In this sense, we subscribe to Isaac Held's viewpoint that the price to pay for adopting models which are overly complex – though (potentially) more "realistic" – with respect to the research question at hand is the risk of reduced understanding [61].

The most compelling issue at this point is to assess the consistency and robustness of the explanation which we have identified. For example: do nonlinear interactions of waves of different spatial scales play an essential role in the onset or the maintenance of low-frequency atmospheric variability? We just mention one amongst the many possible ways for this to occur: the North Atlantic Oscillation (NAO) low-frequency large-scale pattern is found in [62] to result from breaking of synoptic scale waves, where the anticyclonic (cyclonic) wave breakings evolve into the positive (negative) NAO phase, also see [63] and references therein.

5. Future work

We summarise some of the many issues for future research work. From the more physical viewpoint:

1. to characterise the physical patterns associated with the regular and irregular waves, in more complex models and further away from the Hopf bifurcations;
2. to investigate nonlinear wave–wave interactions in a simple modelling framework, incorporating a few, carefully selected spatial scales beyond the planetary wavenumber 3 considered here;
3. to analyse the energy cycle of the waves along the lines of [64], see e.g. [65];
4. to analyse the relation between multimodal statistics and the intermittency scenarios identified here.

In this study we also did not touch a large number of important issues of a more computational and mathematical nature. An open point is the structure near the organising centres of the bifurcation diagram, particularly the Hopf-saddle-node bifurcation of periodic orbits (see Fig. 1). Near this point, a number of gaps interrupts the Hopf–Neĭmark–Sacker bifurcation curve and it is unclear whether the gaps are related to (strong) resonances or to a global mechanism as in [39].

Reduction of infinite-dimensional systems to finite-dimensional systems is a challenging problem. On the one hand there are computational procedures such as discretisation by means of finite differences or Galerkin-like projections. On the other hand there exist conceptual reductions to lower-dimensional models such as restrictions to invariant manifolds containing attractors. However, often the available theorems are not constructive. The challenge lies in reconciling the computational methods with the conceptual methods. The study presented in this paper is a first step in the coherent analysis of the (infinite-dimensional) shallow-water model. There are two important open questions.

1. Which dynamical features of the low-order model persist as the number of retained Fourier modes is increased in the Galerkin projection?
2. Which dynamical features of the low-order model persist in the infinite-dimensional shallow-water model?

For the first, one can think of the approach used in [35–37] for a Rayleigh–Bénard convection problem. A strongly related issue is the investigation of models with an increasing number of layers in the vertical direction.

A rigorous mathematical investigation of the infinite-dimensional system should be undertaken together with computational work. For example, what is the state space of the infinite-dimensional model generated by the equations (5)? Answering this question requires proving the existence of (weak) solutions. The idea would be to follow the methods used for the 2-dimensional Navier–Stokes equations and certain reaction–diffusion equations, see [66,67]. For these equations the Galerkin method is used to construct a sequence of successive approximations which converge to a solution of the weak form of the equations in a suitable Hilbert space. This Hilbert space then serves as a suitable state space on which an evolution operator can be defined. When this has been achieved one can try to prove the existence of finite-dimensional global attractors or inertial manifolds.

Appendix A. Numerical methods

The numerical investigation of the low-order model consists of a mixture of different techniques, which are described briefly in this section. We mainly used the AUTO–07p software [42] to compute the bifurcation curves (e.g. the bottom panel of Fig. 1). Most of the theoretical and computational aspects underlying this software are described in [38]. We have written tailored software for the numerical integration and the computation of Lyapunov exponents (e.g. the top panel of Fig. 1). Our algorithms are sketched below.

A.1. Numerical integration

The low-order model can be written symbolically as

$$\frac{\mathrm{d}x_i}{\mathrm{d}t} = C_i + \sum_{j=1}^{d} L_{ij}x_j + \sum_{j,k=1}^{d} Q_{ijk}x_jx_k, \quad i = 1, \ldots, d. \tag{A.1}$$

This system is integrated numerically by computing a truncated Taylor expansion of the solution around time t_0:

$$x_i(t_0 + h) = \sum_{n=0}^{N} x_i^{[n]}(t_0)h^n + O(h^{N+1}),$$

where the coefficients are given by

$$x_i^{[n]}(t_0) := \frac{1}{n!} \frac{\mathrm{d}^n x_i}{\mathrm{d}t^n}\bigg|_{t=t_0}. \tag{A.2}$$

Given a point $x_i^{[0]}(t_0)$, which is either an initial condition or a previously computed point on the trajectory, we first compute

$$x_i^{[1]} = C_i + \sum_{j=1}^{d} L_{ij}x_j^{[0]} + \sum_{j,k=1}^{d} Q_{ijk}x_j^{[0]}x_k^{[0]}.$$

Then, for $n > 0$, we have the recurrent relation

$$x_i^{[n+1]} = \frac{1}{n+1} \left(\sum_{j=1}^{d} L_{ij}x_j^{[n]} + \sum_{j,k=1}^{d} \sum_{m=0}^{n} Q_{ijk}x_j^{[m]}x_k^{[n-m]} \right),$$

which follows by substituting the truncated Taylor series in (A.1) using the Leibniz rule for differentiation of products.

We have chosen a tolerance $\epsilon = 10^{-16}$. This gives $N = 20$ as the optimal order. The step size is then computed as $h_m = \min\{s_{m,1}, s_{m,2}\}$, where

$$s_{m,1} = \exp\left\{ \frac{1}{N-1} \log\left(\epsilon \frac{\|x^{[1]}\|_\infty}{\|x^{[N]}\|_\infty} \right) \right\},$$

$$s_{m,2} = \exp\left\{ \frac{1}{N-2} \log\left(e^2\epsilon \frac{\|x^{[1]}\|_\infty}{\|x^{[N-1]}\|_\infty} \right) \right\}.$$

A very convenient aspect of the Taylor integration method is the possibility of producing dense output. By choosing step sizes smaller than the one given above, one can compute points along the orbits for any value of t.

For a more detailed account on the Taylor method, see [68].

A.2. Computation of Lyapunov exponents

We compute Lyapunov exponents by means of the algorithm described in [69,70]. To compute the first k Lyapunov exponents we choose at random a set of k orthonormal vectors $v_{1,0}, \ldots, v_{k,0}$. Then we simultaneously integrate the vector field and the first variational equations:

$$\frac{\mathrm{d}x}{\mathrm{d}t} = f(x),$$

$$\frac{\mathrm{d}v_i}{\mathrm{d}t} = D_xf(x(t))v_i, \quad i = 1, \ldots, k.$$

Starting from the initial condition, we integrate the extended system for T units of time. This gives the vectors $x(T)$ and $v_i(T)$. During the integration the vectors $v_i(t)$ tend to align themselves along the direction of maximal expansion. To prevent the vectors v_i from collapsing onto one direction, a Gram–Schmidt procedure is applied to the vectors $v_1(T), \ldots, v_k(T)$, which results in a set of orthogonal vectors $\tilde{v}_1(T), \ldots, \tilde{v}_k(T)$. Then we replace the vectors $v_i(T)$ by the normalised vectors $\tilde{v}_i(T)/\|\tilde{v}_i(T)\|$. Next, we integrate again for T units of time using $x(T)$ and the normalised vectors as

initial conditions. Repeating this procedure N times results in the following estimates for the Lyapunov exponents:

$$\lambda_i = \frac{1}{NT} \sum_{n=1}^{N} \log\left(\|\widetilde{v}_i(nT)\|\right), \quad i = 1, \ldots, k. \tag{A.3}$$

For different methods to compute Lyapunov exponents, see [71,72].

A.3. Visualisation of attractors

The attractors of the low-order model live in a 46-dimensional space, and they have to be projected on a 2-dimensional subspace for visualisation: we use here the directions of maximal amplitude along the orbits (unless otherwise specified). These directions are computed by integrating the variational equations along the trajectory [46].

A.4. Computation of power spectra

By integrating the vector field we obtain a time series $(c_k)_{k=0}^{N-1}$ by measuring the L^2-norm of the solution at regular time intervals. In the power spectra in this paper the solutions have been sampled at time steps of $1/2$.

From this time series we compute a discrete Fourier transform (DFT) by

$$\widehat{c}_k = \frac{1}{N} \sum_{n=0}^{N-1} c_n \exp\left(-2\pi i \frac{nk}{N}\right). \tag{A.4}$$

The power spectrum is a plot of $|\widehat{c}_k|^2$ against the Fourier frequency $f_k = k/N$.

Before computing a power spectrum is computed, the mean is subtracted from the time series:

$$u_k = c_k - \frac{1}{N} \sum_{n=0}^{N-1} c_n.$$

Moreover, a Hamming window is applied to reduce leakage of frequencies. Define the array $(H_k)_{k=0}^{N-1}$ by

$$H_k = 0.54 - 0.46 \cos\left(\frac{2\pi k}{N}\right),$$

and set $v_k = H_k u_k$. The DFT is computed from the array $(v_k)_{k=0}^{N-1}$, and the resulting array $(\widehat{v}_k)_{k=0}^{N-1}$ is normalised by dividing by the norm of the array $(H_k)_{k=0}^{N-1}$.

All frequencies are computed modulo 1. Due to the discrete sampling procedure, all other frequencies are shifted within the interval $[0, 1)$, a phenomenon referred to as aliasing. Moreover, since our time series is real-valued, its DFT is symmetric around the frequency $f = 1/2$. Indeed, from (A.4) it follows that $\widehat{c}_{N-k} = \widehat{c}_k^*$.

The DFT is computed by means of a fast Fourier transform implemented in the FFTW library [73].

Appendix B. Coefficients of the low-order model

In the Galerkin projection the fields u_ℓ, v_ℓ, and h_ℓ are replaced by the truncated Fourier expansions. The resulting equations are multiplied with the basis functions and integrated over the spatial domain. This gives a set of ordinary differential equations for the time-dependent expansion coefficients.

The coefficients in the equations for the low-order model are given by integrals of (products of) the basis functions, which are readily implemented in an algebraic manipulation program. We only present formulas for the projection of terms in the equation for $\widehat{u}_\ell$ onto the basis function $c_{2m}(x; a)c_n(y; b)$. The projection of other terms are given by similar formulas. In the formulas that follow, all integrations are over the rectangle $\Omega = [0, a] \times [0, b]$.

Constant terms

These terms consist of the forcing and topography. Projection of the forcing term gives

$$\iint u_\ell^*(x, y)c_{2m}(x; a)c_n(y; b)\mathrm{d}x\mathrm{d}y.$$

Projection of the topography term gives

$$\iint h_b(x, y)c_{2m}(x; a)c_n(y; b)\mathrm{d}x\mathrm{d}y.$$

Linear terms

The linear terms are due to the pressure gradient, Coriolis force terms, dissipation, and damping terms. Projection of the term

$$\frac{\rho_1}{\rho_0} F \frac{\partial h_1}{\partial x}$$

gives

$$\frac{\rho_1}{\rho_0} F \sum \widehat{h}_{1,p,q}^c \iint c_{2p}'(x; a)c_q(y; b)c_{2m}(x; a)c_n(y; b)\mathrm{d}x\mathrm{d}y$$

$$+ \widehat{h}_{1,p,q}^s \iint s_{2p}'(x; a)c_q(y; b)c_{2m}(x; a)c_n(y; b)\mathrm{d}x\mathrm{d}y.$$

Projection of Coriolis term

$$(Ro^{-1} + \beta y)v_\ell$$

gives the terms

$$\sum Ro^{-1}\widehat{v}_{\ell,p,q}^c \iint c_{2p}(x; a)s_q(y; b)c_{2m}(x; a)c_n(y; a)\mathrm{d}x\mathrm{d}y$$

$$+ \beta\widehat{v}_{\ell,p,q}^c \iint c_{2p}(x; a)s_q(y; b)c_{2m}(x; a)c_n(y; a)y\mathrm{d}x\mathrm{d}y$$

$$+ Ro^{-1}\widehat{v}_{\ell,p,q}^s \iint s_{2p}(x; a)s_q(y; b)c_{2m}(x; a)c_n(y; a)\mathrm{d}x\mathrm{d}y$$

$$+ \beta\widehat{v}_{\ell,p,q}^s \iint s_{2p}(x; a)s_q(y; b)c_{2m}(x; a)c_n(y; a)y\mathrm{d}x\mathrm{d}y.$$

Projection of the Laplace diffusion term

$$Ro^{-1}E_H \Delta u_\ell$$

gives

$$Ro^{-1}E_H \sum \widehat{u}_{\ell,p,q}^c \iint [c_{2p}''(x; a)c_q(y; b)$$

$$+ c_{2p}(x; a)c_q''(y; b)]c_{2m}(x; a)c_n(y; b)\mathrm{d}x\mathrm{d}y$$

$$\widehat{u}_{\ell,p,q}^s \iint [s_{2p}''(x; a)c_q(y; b)$$

$$+ s_{2p}(x; a)c_q''(y; b)]c_{2m}(x; a)c_n(y; b)\mathrm{d}x\mathrm{d}y.$$

Finally, projection of the damping term

$$-\sigma(\mu + \delta_{\ell,2}r)u_\ell$$

gives

$$-\sigma(\mu + \delta_{\ell,2}r) \sum \widehat{u}_{\ell,p,q}^c \widehat{u}_{\ell,m,n}^c$$

$$\times \iint c_{2p}(x; a)c_q(y; b)c_{2m}(x; a)c_n(y; b)\mathrm{d}x\mathrm{d}y$$

$$+ \widehat{u}_{\ell,p,q}^c \widehat{u}_{\ell,m,n}^s \iint s_{2p}(x; a)c_q(y; b)c_{2m}(x; a)c_n(y; b)\mathrm{d}x\mathrm{d}y.$$

$$\sum \widehat{u}_{\ell,p,q}^{c} \widehat{u}_{\ell,r,s}^{c} \iint c_{2p}(x; a) c_q(y; b) c'_{2r}(x; a) c_s(y; b) c_{2m}(x; a) c_n(y; b) \mathrm{d}x\mathrm{d}y$$

$$+ \widehat{u}_{\ell,p,q}^{c} \widehat{u}_{\ell,r,s}^{s} \iint c_{2p}(x; a) c_q(y; b) s'_{2r}(x; a) c_s(y; b) c_{2m}(x; a) c_n(y; b) \mathrm{d}x\mathrm{d}y$$

$$+ \widehat{u}_{\ell,p,q}^{s} \widehat{u}_{\ell,r,s}^{c} \iint s_{2p}(x; a) c_q(y; b) c'_{2r}(x; a) c_s(y; b) c_{2m}(x; a) c_n(y; b) \mathrm{d}x\mathrm{d}y$$

$$+ \widehat{u}_{\ell,p,q}^{s} \widehat{u}_{\ell,r,s}^{s} \iint s_{2p}(x; a) c_q(y; b) s'_{2r}(x; a) c_s(y; b) c_{2m}(x; a) c_n(y; b) \mathrm{d}x\mathrm{d}y$$

Box I.

Quadratic terms

The nonlinear terms in the low-order model are due to the nonlinear advection operator in the original governing equations. For example, the projection of the term

$$u_\ell \frac{\partial u_\ell}{\partial x}$$

gives the terms in Box I in the low-order model, where the summation runs over all pairs (p, q), $(r, s) \in R$.

References

[1] R.M. Dole, Persistent anomalies of the extratropical Northern Hemisphere wintertime circulation, in: B.J. Hoskins, R.P. Pearce (Eds.), Large-Scale Dynamical Processes in the Atmosphere, Elsevier, New York, 1983, pp. 95–109.

[2] F. Baur, Extended range weather forecasting, in: Compendium of Meteorology, Amer. Meteor. Soc, Boston, Massachussets, 1951, pp. 814–833.

[3] D.F. Rex, Blocking action in the middle troposphere and its effect upon regional climate. Part 2: The climatology of blocking action, Tellus 2 (1950) 275–301.

[4] B. Reinhold, Weather regimes—The challenge in extended-range forecasting, Science 235 (4787) (1987) 437–441.

[5] S. Corti, F. Molteni, T.N. Palmer, Signature of recent climate change in frequencies of natural atmospheric circulation regimes, Nature 398 (1999) 799–802.

[6] T.N. Palmer, F.J. Doblas-Reyes, A. Weisheimer, M.J. Rodwell, Toward seamless prediction: Calibration of climate change projections using seasonal forecasts, Bull. Am. Meteor. Soc. 89 (4) (2008) 459–470.

[7] V. Lucarini, S. Calmanti, A. dell'Aquila, P.M. Ruti, A. Speranza, Intercomparison of the northern hemisphere winter mid-latitude atmospheric variability of the IPCC models, Clim. Dyn. 28 (7–8) (2007) 829–848.

[8] A.R. Hansen, A. Sutera, On the probability density distribution of planetary-scale atmospheric wave amplitude, J. Atmos. Sci. 43 (1986) 3250–3265.

[9] R. Benzi, A. Speranza, A. Sutera, A minimal baroclinic model for the statistical properties of low-frequency variability, J. Atmos. Sci. 43 (1986) 2962–2967.

[10] J.G. Charney, J.G. DeVore, Multiple flow equilibria in the atmosphere and blocking, J. Atmos. Sci. 36 (1979) 1205–1216.

[11] B. Legras, M. Ghil, Persistent anomalies, blocking and variations in atmospheric predictability, J. Atmos. Sci. 42 (1985) 433–471.

[12] D.T. Crommelin, Homoclinic dynamics: A scenario for atmospheric ultralow-frequency variability, J. Atmos. Sci. 59 (9) (2002) 1533–1549.

[13] D.T. Crommelin, Regime transitions and heteroclinic connections in a barotropic atmosphere, J. Atmos. Sci. 60 (2) (2003) 229–246.

[14] D.T. Crommelin, J.D. Opsteegh, F. Verhulst, A mechanism for atmospheric regime behaviour, J. Atmos. Sci. 61 (12) (2004) 1406–1419.

[15] P. Malguzzi, A. Speranza, A. Sutera, R. Caballero, Nonlinear amplification of stationary Rossby waves near resonance, Part I, J. Atmos. Sci. 53 (1996) 298–311.

[16] M.H.P. Ambaum, Unimodality of wave amplitude in the northern hemisphere, J. Atmos. Sci. 65 (2008) 1077–1086.

[17] G. Nitsche, J.M. Wallace, C. Kooperberg, Is there evidence of multiple equilibria in planetary wave amplitude statistics? J. Atmos. Sci. 51 (1994) 314–322.

[18] D.B. Stephenson, A. Hannachi, A. O'Neil, On the existence of multiple climate regimes, Quart. J. Roy. Met. Soc. 130 (2004) 583–605.

[19] R. Benzi, A. Speranza, Statistical properties of low frequency variability in the Northern Hemisphere, J. Climate 2 (1989) 367–379.

[20] A.R. Hansen, A. Sutera, The probability density distribution of planetary-scale atmospheric wave amplitude revisited, J. Atmos. Sci. 52 (1995) 2463–2472.

[21] K. Mo, M. Ghil, Cluster analysis of multiple planetary flow regimes, J. Geophys. Res. 93 (1988) 10927–10952.

[22] P.M. Ruti, V. Lucarini, A. dell'Aquila, S. Calmanti, A. Speranza, Does the subtropical jet catalyze the midlatitude atmospheric regimes? Geophys. Res. Lett. 33 (L06814) (2006) 4 pp.

[23] K. Fraedrich, H. Böttger, A wavenumber-frequency analysis of the 500 mb geopotential at 50°N, J. Atmos. Sci 35 (4) (1978) 745–750.

[24] H. Itoh, An observational study of the amplification of the planetary waves in the troposphere, J. Meteor. Soc. Jpn. 61 (1983) 568–589.

[25] R.M. Dole, The life cycles of persistent anomalies and blocking over the North Pacific, Adv. Geophys. 29 (1983) 31–68. R. Benzi, B. Saltzman, A. Wiin-Nielsen (Eds.), Anomalous Atmospheric Flows and Blocking, Academic Press.

[26] J.G. Charney, A. Eliassen, A numerical method for predicting the perturbations of the midlatitude westerlies, Tellus 1 (1949) 38–54.

[27] P. Malguzzi, A. Speranza, A. Sutera, R. Caballero, Nonlinear amplification of stationary Rossby waves near resonance, Part II, J. Atmos. Sci. 54 (1997) 2441–2451.

[28] P.R. Bannon, Quasi-geostrophic frontogenesis over topography, J. Atmos. Sci. 40 (9) (1983) 2266–2277.

[29] P. Cessi, A. Speranza, Orographic instability of nonsymmetric baroclinic flows and nonpropagating planetary waves, J. Atmos. Sci. 42 (1985) 2585–2596.

[30] Y. Pomeau, P. Manneville, Intermittent transition to turbulence in dissipative dynamical systems, Comm. Math. Phys. 74 (1980) 189–197.

[31] H.W. Broer, C. Simó, R. Vitolo, Bifurcations and strange attractors in the Lorenz-84 climate model with seasonal forcing, Nonlinearity 15 (4) (2002) 1205–1267.

[32] V. Lucarini, A. Speranza, R. Vitolo, Parametric smoothness and self-scaling of the statistical properties of a minimal climate model: What beyond the mean field theories? Physica D 234 (2) (2007) 105–123.

[33] H.E. de Swart, Analysis of a six-component atmospheric spectral model: Chaos, predictability and vacillation, Physica D 36 (1989) 222–234.

[34] L. van Veen, Baroclinic flow and the Lorenz–84 model, Int. J. Bifur. Chaos 13 (2003) 2117–2139.

[35] D. Puigjaner, J. Herrero, F. Giralt, C. Simó, Stability analysis of the flow in a cubical cavity heated from below, Phys. Fluids 16 (2004) 3639–3655.

[36] D. Puigjaner, J. Herrero, F. Giralt, C. Simó, Bifurcation analysis of multiple steady flow patterns for Rayleigh–Bénard convection in a cubical cavity at $Pr = 130$, Phys. Rev. E 73 (2006) 046304.

[37] D. Puigjaner, J. Herrero, C. Simó, F. Giralt, Bifurcation analysis of steady Rayleigh–Bénard convection in a cubical cavity with conducting sidewalls, J. Fluid Mechanics 598 (2008) 393–427.

[38] Yu.A. Kuznetsov, Elements of Applied Bifurcation Theory, 3rd edition, Springer, 2004.

[39] H.W. Broer, C. Simó, R. Vitolo, Hopf saddle-node bifurcation for fixed points of 3D-diffeomorphisms: Analysis of a resonance 'bubble', Physica D 237 (13) (2008) 1773–1799.

[40] H.W. Broer, C. Simó, R. Vitolo, The Hopf–Saddle–Node bifurcation for fixed points of 3D-diffeomorphisms: the Arnol'd resonance web, Bull. Belgian Math. Soc. Simon Stevin 15 (5) (2008) 769–787.

[41] E.N. Lorenz, Attractor sets and quasi-geostrophic equilibrium, J. Atmos. Sci. 37 (1980) 1685–1699.

[42] E.J. Doedel, B.E. Oldeman, AUTO–07p: continuation and bifurcation software for ordinary differential equations, Concordia University, Montreal, Canada.

[43] H.W. Broer, G.B. Huitema, M.B. Sevryuk, Quasi-Periodic Motions in Families of Dynamical Systems, in: LNM, vol. 1645, Springer, 1996.

[44] H.W. Broer, F. Takens, Dynamical Systems and Chaos, Epsilon Uitgaven, 2009.

[45] J. Guckenheimer, P. Holmes, Nonlinear Oscillations, Dynamical Systems, and Bifurcations of Vector Fields, Springer, 1983.

[46] C. Simó, On the analytical and numerical computation of invariant manifolds, in: D. Benest, C. Froeschlé (Eds.), Modern Methods of Celestial Mechanics, ed. Frontières, Paris, 1990, pp. 285–330.

[47] H.W. Broer, C. Simó, J.C. Tatjer, Towards global models near homoclinic tangencies of dissipative diffeomorphisms, Nonlinearity 11 (1998) 667–770.

[48] R.L. Devaney, An Introduction to Chaotic Dynamical Systems, 2nd edition, Westview Press, 1989.

[49] J. Palis, F. Takens, Hyperbolicity and Sensitive Chaotic Dynamics at Homoclinic Bifurcations, Cambridge University Press, 1993.

[50] S. Wieczorek, B. Krauskopf, D. Lenstra, Unnested islands of period doublings in an injected semiconductor laser, Phys. Rev. E 64 (2001) 056204.

[51] H.W. Broer, G.B. Huitema, F. Takens, B.L.J. Braaksma, Unfoldings and bifurcations of quasi-periodic tori, Memoirs of the AMS 83 (1990).

[52] H.W. Broer, R. Roussarie, C. Simó, On the Bogdanov–Takens bifurcation for planar diffeomorphisms, in: C. Perelló, C. Simó, J. Solà-Morales (Eds.), Proc. Equadiff 91, 1993, pp. 81–92.

[53] E. Hovmöller, The trough and ridge diagram, Tellus 1 (1949) 62–66.

[54] H.A. Dijkstra, Nonlinear Physical Oceanography, second revised and enlarged edition, Springer, 2005.
[55] H.A. Dijkstra, Dynamical Oceanography, Springer, 2008.
[56] J.R. Holton, An Introduction to Dynamic Meteorology, 4th edition, Elsevier Academic Press, 2004.
[57] R. Benzi, P. Malguzzi, A. Speranza, A. Sutera, The statistical properties of general atmospheric circulation: observational evidence and a minimal theory of bimodality, Quart. J. Roy. Met. Soc. 112 (1986) 661–674.
[58] H.W. Broer, R. Vitolo, Dynamical systems modelling of low-frequency variability in low-order atmospheric models, DCDS B 10 (2008) 401–419.
[59] A. Majda, C. Franzke, A. Fischer, D. Crommelin, Distinct metastable atmospheric regimes despite nearly Gaussian statistics: A paradigm model, PNAS 103 (22) (2006) 8309–8314.
[60] P. Malguzzi, A. Speranza, Local multiple equilibria and regional atmospheric blocking, J. Atmos. Sci. 38 (1981) 1939–1948.
[61] I.M. Held, The gap between simulation and understanding in climate modeling, Bull. Am. Meteor. Soc. (2005) 1609–1614.
[62] J.J. Benedict, S. Lee, S.B. Feldstein, Synoptic view of the north atlantic oscillation, J. Atmos. Sci. 61 (2004) 121–144.
[63] P.J. Athanasiadis, M.H.P. Ambaum, Do high-frequency eddies contribute to low-frequency teleconnection tendencies? J. Atmos. Sci. 67 (2010) 419–433.
[64] E.N. Lorenz, The nature and theory of the general circulation of the atmosphere, World Meteorological Organization, No. 218, TP 115, 1967, 161 pp. Available at http://eapsweb.mit.edu/research/Lorenz/publications.htm.
[65] A. Speranza, P. Malguzzi, The statistical properties of a zonal jet in a baroclinic atmosphere: A semilinear approach. Part I: Two-layer model atmosphere, J. Atmos. Sci. 45 (1988) 3046–3061.
[66] J.C. Robinson, Infinite-Dimensional Dynamical Systems, Cambridge University Press, 2001.
[67] R. Temam, Infinite-Dimensional Dynamical Systems in Mechanics and Physics, Springer, 1997.
[68] À. Jorba, M. Zou, A software package for the numerical integration of ODEs by means of high-order Taylor methods, Exper. Math. 14 (2005) 99–117.
[69] G. Benettin, L. Galgani, A. Giorgilli, J.-M. Strelcyn, Lyapunov characteristic exponents for smooth dynamical systems and for Hamiltonian systems: A method for computing all of them. Part 1: Theory, Meccanica 15 (1980) 9–20.
[70] G. Benettin, L. Galgani, A. Giorgilli, J.-M. Strelcyn, Lyapunov characteristic exponents for smooth dynamical systems and for Hamiltonian systems: A method for computing all of them. Part 2: Numerical application, Meccanica 15 (1980) 21–30.
[71] L. Dieci, R.D. Russel, E.S. van Vleck, On the computation of Lyapunov exponents for continuous dynamical systems, SIAM J. Numer. Anal. 34 (1997) 402–423.
[72] L. Dieci, Jacobian free computation of Lyapunov exponents, J. Dynam. Differential Equations 14 (2002) 697–717.
[73] M. Frigo, S.G. Johnson, The design and implementation of FFTW3, Proceedings of the IEEE 93 (2005) 216–231.